

Dedicated holmium microsphere administration device for MRI-guided interstitial brain microbrachytherapy

de Vries, M.; Klaassen, N. J.M.; Morsink, N. C.; van Nimwegen, S. A.; Nijsen, J. F.W.; van den Dobbelaars, J. J.

DOI

[10.1016/j.medengphy.2021.07.009](https://doi.org/10.1016/j.medengphy.2021.07.009)

Publication date

2021

Document Version

Final published version

Published in

Medical engineering & physics

Citation (APA)

de Vries, M., Klaassen, N. J. M., Morsink, N. C., van Nimwegen, S. A., Nijsen, J. F. W., & van den Dobbelaars, J. J. (2021). Dedicated holmium microsphere administration device for MRI-guided interstitial brain microbrachytherapy. *Medical engineering & physics*, 96, 13-21.
<https://doi.org/10.1016/j.medengphy.2021.07.009>

Important note

To cite this publication, please use the final published version (if applicable).
Please check the document version above.

Copyright

Other than for strictly personal use, it is not permitted to download, forward or distribute the text or part of it, without the consent of the author(s) and/or copyright holder(s), unless the work is under an open content license such as Creative Commons.

Takedown policy

Please contact us and provide details if you believe this document breaches copyrights.
We will remove access to the work immediately and investigate your claim.



Dedicated holmium microsphere administration device for MRI-guided interstitial brain microbrachytherapy

M. de Vries^{a,*}, N.J.M. Klaassen^b, N.C. Morsink^c, S.A. van Nimwegen^c, J.F.W. Nijssen^{b,d}, J. J. van den Dobbelsteen^a

^a Department of BioMechanical Engineering, Faculty of Mechanical, Maritime and Materials Engineering, Delft University of Technology, Mekelweg 2, Delft 2628 CD, the Netherlands

^b Department of Medical Imaging, Radboud Institute for Health Sciences, Radboud university Medical Center, Geert Grooteplein Zuid 10, Nijmegen 6525 GA, the Netherlands

^c Department of Clinical Sciences, Faculty of Veterinary Medicine, Utrecht University, Yalelaan 108, Utrecht 3508 TD, the Netherlands

^d Quirem Medical B.V., Zutphenseweg 55, Deventer 7418 AH, the Netherlands

ARTICLE INFO

Keywords:

Image-guided
Brachytherapy
Brain tumour
Steerable needle
Holmium

ABSTRACT

Microbrachytherapy with radioactive holmium-166 (¹⁶⁶Ho) microspheres (MS) has the potential to be an effective treatment method for brain malignancies. Direct intratumoural delivery of ¹⁶⁶Ho-MS and dose coverage of the whole tumour are crucial requirements. However, currently no dedicated instruments for controlled intratumoural delivery exist. This study presents an administration device that facilitates this novel magnetic resonance imaging (MRI) -guided intervention. The bioceramic alumina oxide cannula creates a straight channel for a superelastic nitinol precurved stylet to control spatial deposition of Ho-MS. End-point accuracy of the stylet was measured during insertions in phantoms. Imaging tests were performed in a 3 Tesla MRI-scanner to quantify instrument-induced artefacts. Additionally, the feasibility of non-radioactive holmium-165 (¹⁶⁵Ho)-MS delivery with the administration device was evaluated in a brain tumour simulant. Absolute stylet tip error was 0.88 ± 0.61 mm, instrument distortion in MRI depended on needle material and orientation and dose delivery of ¹⁶⁵Ho-MS in a brain tumour phantom was possible. This study shows that the administration device can accurately place the stylet for injection of Ho-MS and that visualization can be performed with MRI.

1. Introduction

Worldwide, the incidence of brain malignancies is approximately 300.000 patients each year [1]. Although the chance on long-term survival is generally small, specific treatment can be of great value [2–4]. Neurosurgery is traditionally performed for solid malignancies and whole-brain radiotherapy is used for treatment of multiple brain metastases with a median survival of 11.6 months [5]. Chemotherapy can be used depending on location, size and number of tumours. The efficacy of these, generally, palliative procedures is highly dependent on several factors including, but not limited to, imaging accuracy, dosimetry for radiotherapy treatment, and the blood-brain barrier (BBB) for chemotherapy treatment. Brachytherapy, a minimally invasive treatment with radioactive implants often containing Iodine-125, can be used for treatment of brain tumours. This technique bypasses the BBB and may be beneficial in a highly selected patient group. Nevertheless, permanent

low,- and temporary high-activity radionuclide implants showed unfavourable outcomes with respect to radiation necrosis and reoperation rate [6,7].

Holmium-166 (¹⁶⁶Ho) is seen as a suitable isotope for internal radiotherapy and is characterized by a short half-life time of 26.8 hours and a high energy beta emission [8–11]. The beta-particles could damage the cancer cell's DNA and prevent the cells from reproducing [10, 12]. The beta radiation with an energy of 1.84 MeV will have a maximum tissue range of 8.7 mm. Ninety percent of the beta radiation is absorbed in the adjacent 2.1 mm of tissue around the point of deposition (mean penetration depth: 2.2 mm) [13]. ¹⁶⁶Ho also emits low energy gamma-rays which can be used for nuclear imaging [14]. Furthermore, ¹⁶⁶Ho is highly paramagnetic and has a high mass attenuation coefficient making it suitable for imaging with MRI and CT [15,16]. Delivery of the radionuclides is ensured by microspheres suspended in a carrier fluid, therefore terming the procedure microbrachytherapy.

* Corresponding author.

E-mail address: M.devries-2@tudelft.nl (M. de Vries).

<https://doi.org/10.1016/j.medengphy.2021.07.009>

Received 27 November 2020; Received in revised form 15 July 2021; Accepted 21 July 2021

Available online 12 August 2021

1350-4533/© 2021 The Author(s). Published by Elsevier Ltd on behalf of IPPEM. This is an open access article under the CC BY license

(<http://creativecommons.org/licenses/by/4.0/>).

Direct delivery of radioactive ^{166}Ho -MS in brain tumours looks promising [8,10], as it minimizes toxicity to surrounding healthy tissue while the irradiation dose to the tumour can be high [17,18]. MRI is considered as a promising visualization method for this application. MRI shows high tissue contrast and allows for anatomical tumour reference in combination with quantitative distribution of the injected radioactive (^{166}Ho) and non-radioactive (^{165}Ho) microspheres [18]. Nevertheless, reaching the whole tumour with a lethal radiation dose is crucial to obtain efficacy [15] and reduce local recurrence [6,19]. Currently, no dedicated needle systems exist for controlled administration of Ho-MS under MRI guidance. Normal straight syringes lack the ability to distribute the Ho-MS over the whole tumour and multiple punctures through healthy brain parenchyma are not desirable as it may increase risk of haemorrhage and dissemination of cancer cells [20,21].

Multiple scientific studies have described the use of conventional straight rigid needles in minimally invasive procedures and reported the potential benefits of steerable needles for controlled and local administration of fluids and suspensions [21–27]. Needle steering can be introduced by tendon wires, pushing rods, external mechanisms or lateral forces acting on the tip during insertion into tissue [26]. Bevel-tipped steering was suggested for needle steering in brain tissue in earlier studies [22,25,28]. But, this approach involves nonholonomic constraints which complicates needle tip control [29]. Within this work, steering of the needle is accomplished by mechanical energy stored in the configuration of the instrument. The design is composed of two concentric tubes of which the inner needle has a circular precurvature in line with previously described needles [23,24,26,30]. The tip of the curvature can be directed to a region in the tumour where Ho-MS can be injected following a planned path and place. This solution potentially contemplates only damage of healthy brain tissue along the length of the cannula, while reach within the tumour can be enlarged or multiple locations in the brain can be targeted.

This work presents a three degrees of freedom (DoF) Ho-MS administration device intended for MRI-guided interstitial brachytherapy of brain tumours. The mechanism on the proximal end of the instrument decouples translation and rotation of the stylet and movements can be controlled separately to locally inject the Ho-MS suspension in malignant brain tissue. Patients normally treated by stereotactic radiosurgery (SRS) were considered as potentially eligible candidates for interstitial Ho-MS microbrachytherapy in the future, as SRS is limited to lesions of 30 mm [31]. Therefore, a spherical tumour with a diameter of 30 mm is used as base for the instrument design. The developed prototype is validated on positioning accuracy of the stylet in gelatin phantoms and on dose delivery capability with Ho-MS in tissue phantoms mimicking a tumour in brain tissue. Next to mechanical and dose distribution performance, artefact quantification of the instrument is studied in a 3 Tesla MRI test.

2. Materials and methods

2.1. Instrument design

The mechanical design of the instrument allows for manual control of the axial translation (DoF 1) and axial rotation (DoF 2) of the stylet to accurately target an entire lesion of 30 mm in diameter and distribute Ho-MS locally. Deeper instrument insertions are realized by axial translation of the cannula (DoF 3). Intraprocedural visualization and localization of the instrument with MRI should be possible, which entails the criteria of non-ferromagnetic materials. The proximal end of the stylet should allow for syringe attachment and both depth and orientation indicators should inform the physician about the stylet position.

Figs. 1 and 2 show the developed administration device. It consists of three main components: (1) a straight outer needle, referring to as cannula, creating a tumour-extracorporeal working channel for (2) the inner needle, known as the stylet. The stylet has a precurved tip on the distal end which will be straight when positioned inside the cannula.

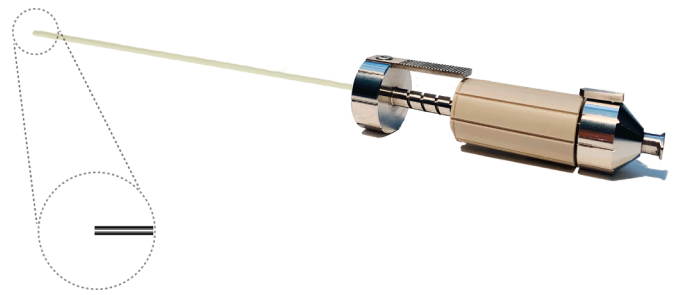


Fig. 1. Administration device with stylet in initial position. Cross-section of the stylet tip is enlarged in the bottom left.

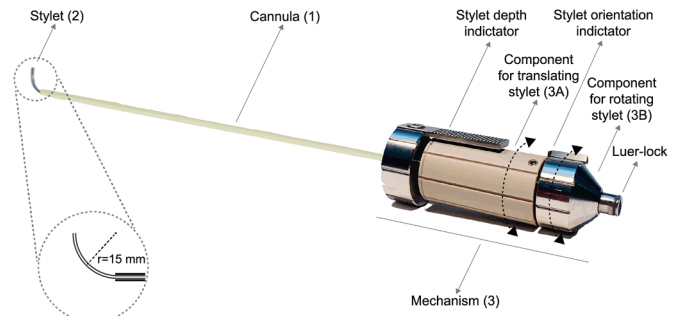


Fig. 2. Administration device with stylet in maximum position. Black arrows indicate intended rotational movement to control stylet translation and rotation. Components are identified by the grey arrows, text and numbers. Cross-section of the stylet tip is enlarged in the bottom left.

Rotation and translation of the stylet can be separately controlled by (3) the mechanism on the proximal end of the instrument. Insertion of the cannula towards the lesion should be done in the initial stylet position, meaning that the distal end of both the stylet and cannula are in the same plane (see Fig. 1). The component at the handle for translating the stylet (component 3A) allows for longitudinal movement, eventually reaching the maximum position of the stylet, shown in Fig. 2. By rotating the stylet inside the cannula (using component 3B) the right orientation for reaching a target can be set. Rotation is done inside the cannula to prevent tissue damage. Following this procedure, multiple locations in the tumour can be targeted with only one puncture through the healthy brain parenchyma. In this way, the instrument bypasses the blood brain barrier and minimizes damage to intermediate structures.

2.1.1. Cannula

The 200 mm stiff cannula has an inner and outer diameter of 0.8 mm and 1.6 mm respectively and is manufactured from the bioceramic material alumina oxide (Al_2O_3 , 99.8% purity) (Ortech Ceramics, Sacramento, California, USA). Al_2O_3 has optimal properties for this application: biocompatibility [32–34], low magnetic susceptibility ($\chi_{\text{alumina}} = -18.1 \times 10^{-6}$) in MRI scans [35,36], high material stiffness ($E_{\text{mod}} = \sim 370$ GPa) [37] and scratch resistance [32–34]. Both empirical tests and material availability resulted in an instrument's outer diameter of 1.6 mm, which is below the diameter of biopsy needles currently used for brain tumour diagnosis [38]. In this way, an optimum is found between minimizing damage to the patient's healthy brain tissue along the insertion length and withstanding the force the precurved stylet tip exerts on the inside of the cannula, retaining its straight path. Finite element analysis in ABAQUS/CAE 2017, described in Section 2.1.4, is performed to analyse the used dimensions and to show other adequate dimensional values. During microbrachytherapy the cannula with blunt distal tip is advanced through a cranial burr-hole and a channel to the periphery of the tumour is created. This channel overcomes transition between tissue layers potentially inducing deformation when inserting the stylet [39].

2.1.2. Stylet

The stylet is made from superelastic nitinol (SE NiTi, EUROFLEX GmbH, Pforzheim, Germany). This material is reported to be biocompatible, resistant to fatigue and twist, creates small susceptibility artefacts in MRI and is superelastic [40,41]. The magnetic susceptibility value of nitinol is 245×10^{-6} , where human soft tissues are estimated to be in a range of $\sim 20\%$ of $\chi_{\text{water}} = -9.05 \times 10^{-6}$ [36]. The superelastic behaviour allows for a curvature on the distal end of the stylet, which adopts a straight orientation when advanced through the cannula and returns to its precurved shape if the tip comes out of the cannula. This phenomenon is created by a phase transition of the SE NiTi material from martensite, due to the external load of the cannula on the stylet tip, to austenite, having a crystalline structure transformation when there is no induced stress. The inner and outer diameter of respectively 0.42 mm and 0.71 mm match a 22G needle, corresponding to the needle gauge used in earlier experiments with ^{166}Ho [42]. The tip has a curvature with a 15 mm radius over a distance of 0.5π radians. The stylet can be connected to a syringe, containing the Ho-MS suspension, via a luer-lock on the proximal end of the instrument. Passive steering of the stylet can be used to control spatial placement for deposition of the Ho-MS.

2.1.3. Mechanism

Fig. 3 shows the exploded view of the mechanism located on the proximal end of the instrument. The cannula (Fig. 3 A) is connected to the distal part of the mechanism (Fig. 3 B), Component B contains a spiral thread with a pitch of 5 mm in which the pin of component C can move causing axial movement of component C and associated extension of the stylet (component D). Attachment of the component C to component B is accomplished after revolution of π radians of component C. Clockwise rotation of (C), with a maximum of 4 rotations, will cause exposure of the stylet's curvature. To change steering direction of the stylet component D can be rotated over 2π radians. This allows for a deposition of the radioactive nuclides over a maximum circular surface of 7.1 cm^2 . It should be noted that translation and rotation of the stylet can only be controlled individually when the corresponding component is rotated while the other component is gripped at the same time.

2.1.4. Finite element analysis

Analysis of the computational administration device model is performed in ABAQUS/CAE 2017 (Simulia, Johnston, RI, USA). The finite element model is created to study the used parameters of the cannula, other potentially adequate dimensions and stylet behaviour with increasing clearance between the two concentric tubes. Both the cannula and stylet are designed as shell with a given offset from midplane,

described as wall thickness. The shell diameter of the cannula varies from 1.0 to 1.5 mm with a wall thickness ranging from 0.2 to 0.5 mm. A dynamic implicit solver and standard quadratic elements (type S8R5) for discretization of both the cannula and stylet are used in the model. Refined meshing towards the distal tip of the instrument is performed to maximize sensitivity of the results. The cannula is clamped at the proximal end over the first 50 mm, while the stylet is allowed to move through the cannula in longitudinal direction. Interaction between both needles is possible via surface-to-surface contact with a set friction coefficient of 0.15. The mechanical properties of the stylet are retrieved from literature [43].

2.2. Validation experiments

Three tests evaluate the potential of the developed instrument. First, repeatability in stylet accuracy is tested for 12 experimental conditions ($N=96$). Second, an imaging test with 3T MRI is performed and visualization errors of the used materials are determined. Third, proof of principle is demonstrated by injecting $^{165}\text{Ho-MS}$ in a tumour in brain phantom and the dose distribution is measured.

2.2.1. Positioning accuracy

Set-up. The accuracy and precision of stylet insertions are measured in transparent phantom blocks. Porcine gelatin (Gelatine, Dr. Oetker, Bielefeld, Germany) tissue simulant blocks ($50 \times 50 \times 40 \text{ mm}$) of 13 wt. %, approaching the Young's modulus of the stiffest brain tumour tissue found in Abramczyk & Imiela [44] ($E_{\text{mod}} = 75.7 \text{ kPa}$) are prepared and allowed to reach room temperature. The upper part of the cannula is fixed to a linear stage (Aerotech PRO 115, Aerotech Inc., Pittsburgh, PA, USA). The distal tip of the cannula is punctured into a phantom block before extending the stylet to minimize cutting and friction forces acting on the stylet tip during phantom insertion. All trials are performed in new gelatin blocks to avoid the influence of previously created needle paths.

Procedure. The magnitude of the stylet extension is controlled by rotation of the corresponding part on the handle (see Fig. 2). Consecutively, 1, 2, 3 and 4 rotations of component 3A are performed to place the stylet further into the phantom with 5 mm depth per rotation to evaluate depth dependency. The orientation of the stylet can be controlled by component 3B. To determine steering uniformity the set stylet angle is varied between 0° , 90° and 315° .

Data acquisition. Accuracy of the stylet is assessed by a measure of error. Stylet depth and lateral stylet displacement are evaluated after the insertion in a transparent gelatin block and compared to the reference value, defined as target in Fig. 4. The reference value is determined prior to the trials of all experimental conditions without the use of a phantom and the corresponding needle-tissue interaction forces. Pictures, using two 12MP sensor cameras with $1.22 \mu\text{m}$ pixels, in both the XZ- and YZ-plane are taken and processed after every puncture to obtain both depth and lateral error of the stylet tip. In total 96 punctures provided us with 168 instead of 192 end-point locations, as 24 positions were not clearly visible on the pictures and excluded from the study sample. The diameter of the cannula is measured as 30 pixels in the pictures, thus providing a conversion unit from pixels to mm. Coordinates of the stylet tip for each trial in the same experimental condition are averaged and compared to the coordinates of the dry-run for the corresponding condition to obtain the mean error. Absolute error is defined by the Pythagorean formula.

Data analysis. Statistical tests are performed in SPSS Statistics 25 (IBM Corp, Armonk, NY, USA) to analyse the influence of independent variables; orientation angle and stylet depth. A Shapiro-Wilk's test, the

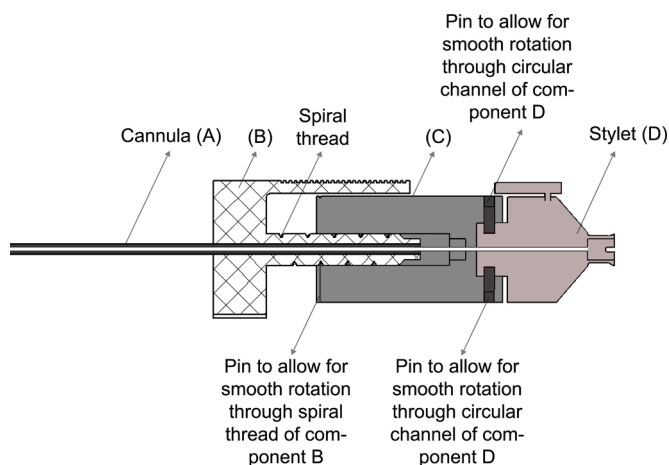


Fig. 3. Cross-section of mechanism at the proximal end of the instrument. Components are identified by the grey arrows, text and letters (A–D). The stylet is positioned in between the initial and maximum position to clearly show the spiral thread of component B.

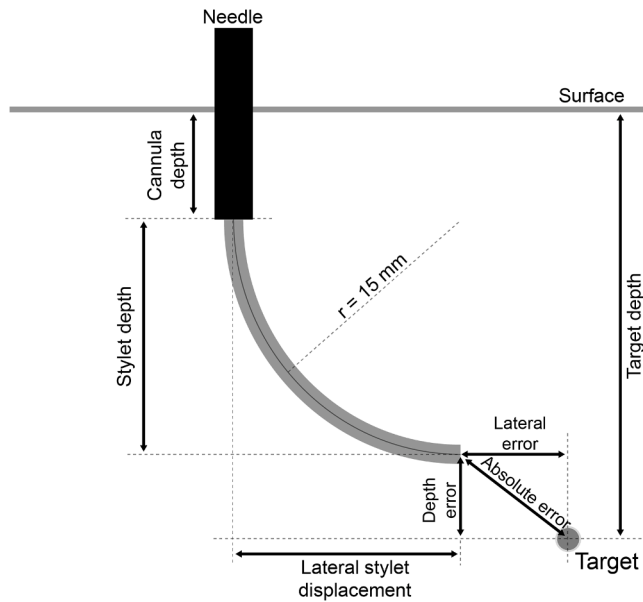


Fig. 4. Schematic of measurements for the positioning accuracy test of the stylet. Here, the stylet is placed in the maximum position, so after 4 rotations of the component allowing for stylet translation.

normal Q-Q plots and a visual inspection of their histograms is performed to verify non-normal error distribution. The nonparametric Levene's and a Kruskal-Wallis test are performed to evaluate mean differences and p -values < 0.05 were considered statistically significant. The average error in the XZ,- and YZ-plane is evaluated. No significant difference is assumed between both planes, as a homogeneous phantom is pierced. Differences in experimental conditions for orientation angle and stylet depth may indicate shortcomings in the instrument design.

2.2.2. Material-induced artefact quantification in MRI

Susceptibility-induced distortions allow for artefact size quantification of the instrument during the procedure. Eq. (1) shows the distortion, where A is the artefact size and s is the corresponding instrument dimension. Noteworthy is that A consists of a hypointense (dark) and hyperintense (bright) part. Both intensities are considered during the calculations as either of them can obscure intracranial structures and abnormalities.

$$\% \text{ Distortion} = \frac{(A - s)}{s} * 100\% \quad (1)$$

Set-up. To determine the instrument-related artefact, the stylet and cannula are placed in a soft gelatin phantom (3 wt.%) and MRI scans are made using a whole-body clinical 3T MRI scanner (MAGNETOM Skyra, Siemens Healthineers, Erlangen, Germany). The phantom is placed in a PMMA container with needle guiding holes in the front surface. For this experiment a stylet is designed and manufactured as a straight tube, in austenite phase, instead of the final curved stylet to easily evaluate the influence of needle orientation on the formation of the artefact. The stylet and cannula have a length of 80 mm and 50 mm, respectively.

Procedure. The Al_2O_3 cannula is placed for 30 mm in the phantom perpendicular orientated towards the longitudinal axis of the static magnetic field (B0), obtaining ultimate measurements for cannula distortions on the MRI. Subsequently, a straight SE NiTi tube with corresponding diameters from Section 2.1.2. is advanced through the cannula for 60 mm. MRI scans are made to show stylet distortion in the first 30 mm when covered by the cannula and in the range between 30 and 60 mm where only stylet distortions will be measured. To investigate dependence on needle orientation towards B0, the phantom and needle

together are placed under different angles in the MRI scanner: 90° , 75° , 60° , 45° , 30° , 15° and 0° .

Data acquisition. T2 weighted turbo spin echo (T2W-TSE) scans are acquired. The imaging parameters were: FOV = $185 \times 180 \text{ mm}$; flip angle = 160° ; bandwidth = 200 Hz; TR/TE = 3500/101 ms; in plane voxel size = $1.09 \times 1.09 \text{ mm}$; slice thickness = 3 mm and number of slices = 19.

Data analysis. DICOM files are processed in RadiAnt DICOM viewer (Medixant, Poznań, Poland) and window width/level is set to 1280/2560 for visualization of the hypointensity and hyperintensity in transverse plane. The susceptibility artefacts are manually measured three times per segment resulting in an average distortion \pm standard deviation ($\pm \sigma$). During the normal procedure, the stylet has a circular curvature over 0.5π radians, thus perpendicular placement of the straight SE NiTi tube in this experiment will match a parallel orientation of the curved stylet tip.

2.2.3. Proof of principle with Ho-MS injection

A feasibility experiment is performed using a phantom mimicking the mechanical and dynamic response of human brain tissue. For safety reasons, the experiment is performed with non-radioactive $^{165}\text{Ho-MS}$, while microbrachytherapy for brain tumours is performed using radioactive $^{166}\text{Ho-MS}$.

Phantom. The phantom is composed of a baseline composite hydrogel (CH) and incorporated a tumour phantom with a diameter of 50 mm. This diameter allows for both stylet and Ho-MS placement over a diameter of 30 mm and Ho-MS penetration in the phantom. The baseline CH was obtained by dissolving 1.125 wt% Polyvinyl Alcohol (PVA) and 0.425 wt% Phytigel in deionized water [45]. 0.0012 wt% Manganese chloride (MnCl_2) was added to mimic the T2 MRI contrast of gray matter and tumour tissue [46]. The brain and tumour phantom have the same material composition but underwent one and two freeze-thaw cycles respectively to obtain differences in elasticity.

Procedure. The phantom is injected nine times with $^{165}\text{Ho-MS}$ (19.6% by mass Holmium-165) suspended in an injection fluid (Ho-MS provided by Quirem Medical, Deventer, The Netherlands), with a concentration of 4 mg Holmium-165/ml fluid. The volume of each injection was 0.3 ml. The phantom injection is done in a standardized manner, starting with a manual insertion of the cannula followed by four injections in four different orientations (0° , 90° , 180° and 270°) with the stylet in maximum position at 17.5 mm from the bottom of the tumour. Subsequently, four injections at a height of 32.5 mm with the stylet in maximum position and one injection at the top of the tumour with the stylet in its initial position were made (Fig. 5). MRI is performed prior to insertion of the instrument, after insertion of the cannula, after exposure of the stylet and after injection of the $^{165}\text{Ho-MS}$. If the needle was not in the preferred position, the position of the stylet was adjusted and MRI was repeated, until the positioning was correct.

Data acquisition. Data is acquired on a whole-body, clinical 3T MRI scanner (MAGNETOM Skyra, Siemens Healthineers, Erlangen, Germany), using a head coil in receiving mode. For instrument placement and location of the tumour T2W-TSE scans are acquired. The imaging parameters were: FOV = $256 \times 256 \text{ mm}$; flip angle = 160° ; bandwidth = 200 Hz; TR/TE = 4670/107 ms; in plane voxel size = $1.09 \times 1.09 \text{ mm}$; slice thickness = 3 mm and number of slices = 17. For the detection and quantification of Ho-MS, a multi-gradient echo sequence is used. The parameters of this sequence were: FOV = $153 \times 379 \text{ mm}$; flip angle = 37° ; bandwidth = 1565 Hz; TR/TE1/ Δ TE = 188/1.13/1.12 ms with 10 echoes; in plane voxel size = $3 \times 3 \text{ mm}$; slice thickness = 3.5 mm and number of slices = 58.

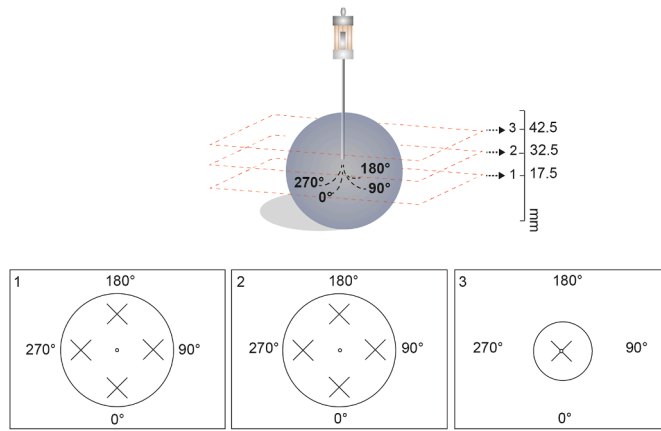


Fig. 5. Injection protocol of the tumour phantom. Three cross-sections in transversal plane at different heights show the Ho-MS injection locations indicated by the cross-marks. Four depots will be placed in four different orientations (0° , 90° , 180° and 270°) at a depth of 17.5 mm from the bottom of the tumour, four at a distance of 32.5 mm from the bottom and one in the central axis at a height of 42.5 mm.

Data analysis. MRI-based dose maps, indicating the nominal dose, are simulated via a commercially available software package Q-suite (Quirem Medical, Deventer, The Netherlands) which uses previously described and validated methods [47,48]. A fictional specific activity of 12 MBq/mg was used for the $^{165}\text{Ho-MS}$ according to the average specific activity used in clinical practice [49].

3. Results

3.1. Finite element analysis

Fig. 6 shows both the Von Mises stress and deflection of the cannula while retracting the stylet into the cannula using a polynomial curve fitting for noise reduction. The deflection of the cannula increases during retraction of the stylet and the von Mises stress is highest when the stylet is positioned in the cannula.

Table 1 and Fig. 7 show the results of twelve determined experimental conditions. The cannula developed in this study (EC 7) shows a maximum deflection at the tip of 0.09 mm and a maximum Von Mises stress of 95.37 MPa. Considering the Modulus of Rupture of Al_2O_3 (~ 375 MPa) [37] the Factor of Safety of the cannula is 3.9. For other experimental conditions, wall thickness (WT) of the cannula and clearance between cannula and stylet are varied. An increase in both wall

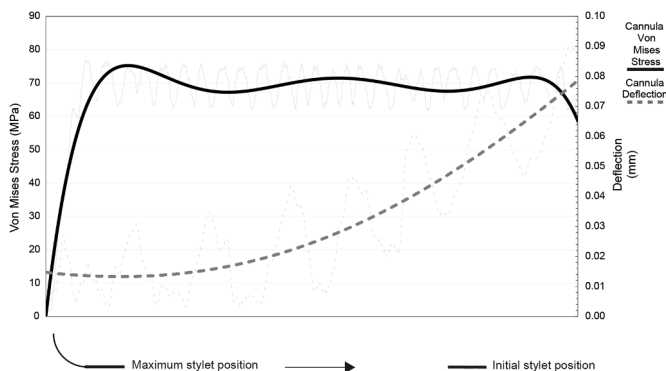


Fig. 6. FEA in ABAQUS showing the Von Mises stress acting upon the cannula and the deflection of the cannula, caused by the force of the curvature of the stylet, during retraction of the stylet through the cannula. Polynomial curve fitting (indicated by thick lines) is used to reduce the noise in the simulation (indicated by thin lines).

thickness and clearance result in a reduction of both the maximum Von Mises stress and maximum deflection of the cannula indicated by the trend line in Fig. 7. Fig. 8 shows the course the stylet makes inside the cannula. Oscillation of the stylet increases with clearance in the needle system and results follow the bending behaviour presented in Okazawa et al. [30].

3.2. Positioning accuracy

Non-normally distributed absolute stylet tip errors were found in IBM SPSS Statistics 25 for all experimental conditions. Table 2 shows the mean absolute error and standard deviation ($\pm \sigma$) for all variables. A Kruskal-Wallis test showed that measurement plane (XZ,- or YZ-plane) did not significantly influence the error obtained ($p > 0.05$). Statistically significant differences in absolute errors were obtained for different stylet depths, $\chi^2(3) = 11.534$, $p = 0.009$, significantly influenced by the vertical component, $\chi^2(3) = 24.014$, $p < 0.001$. Next to this, significantly different absolute errors were found for the set orientation angle, $\chi^2(2) = 10.120$, $p = 0.006$. This error was mainly influenced by the horizontal component, $\chi^2(2) = 41.592$, $p < 0.001$.

3.3. Material-induced artefact quantification in MRI

The bioceramic cannula creates a distortion in the 3T MRI scanner of $80.6 - 104.4 \pm 2.5\%$. Advancing the SE NiTi stylet through the cannula for 60 mm induces a distortion up to $264.6 \pm 13.2\%$ in the first 30 mm. A maximum distortion of $745.1 \pm 22.0\%$ was found for the stylet in the next 30 mm. Fig. 9 shows the hypointense and hyperintense signal of both the cannula and stylet alone and together when oriented perpendicular to B0. The artefact in the first 30 mm, created by the combination of the Al_2O_3 cannula and the SE NiTi stylet, is not different from the signal void of the stylet alone. However, the distortions calculated with Eq. (1) indicate a difference due to the associated dimensions. Fig. 10 gives an overview of the material-induced artefacts found in the 3T MRI test. The effect of needle angle towards B0 is clearly visible for the SE NiTi stylet, where a more perpendicular orientation results in higher distortions. Noteworthy is that in some scans larger distortions were measured at the distal tip.

3.4. Proof of principle with Ho-MS injection

Placement of the stylet was performed in nine different locations within the tumour phantom while only one main channel was created by the cannula. Ho-MS injection was possible in all predefined positions with a distance of ≤ 10 mm to the border of the tumour (Fig. 11, left). Dose distribution of the $^{165}\text{Ho-MS}$ resulted in a total mean dose of 66 Gy, where 40% of the tumour volume received a dose of at least 60 Gy (Fig. 11, right).

4. Discussion

This study describes a novel administration device for MRI-guided radiation therapy of brain malignancies. The instrument, consisting of two concentric tubes, has three DoF and steering arises from mechanical energy stored in the configuration of the instrument. The administration device meets the defined design objectives, where the intended procedure should be performed by a minimum number of instrument insertions through the healthy brain parenchyma while bypassing the blood brain barrier. The diameter of the cannula is smaller compared to the commonly used brain biopsy needles of 1.8 and 2.0 mm [38] potentially minimizing brain damage. Bending stiffness of the rigid alumina oxide cannula can withstand the force exerted by the curvature of the nitinol stylet having a Factor of Safety of 3.9. When advanced out of the cannula, the stylet relaxes into its originally set curvature with a radius of 15 mm. Stylet tip positioning in multiple locations is ensured by the mechanism which allows for dose delivery of $^{165}\text{Ho-MS}$ after. This

Table 1

FEA of cannula in ABAQUS. Twelve experimental conditions are defined, varying in wall thickness (WT) and shell of the cannula. The shell diameter affects the clearance within the needle system. For example a shell of 1.20 mm and a WT of 0.20 mm create an outer diameter of 1.40 mm. All experimental conditions are evaluated on the maximum Von Mises stress and maximum cannula deflection.

		Wall thickness of cannula (mm)											
		0.20 mm			0.30 mm			0.40 mm			0.50 mm		
	EC	Max. Stress (MPa)	Max. deflection (mm)		Max. Stress (MPa)	Max. Deflection (mm)		Max. Stress (MPa)	Max. Deflection (mm)		Max. Stress (MPa)	Max. Deflection (mm)	
Shell of cannula (mm)Shell of	1.00	1	364.9	0.33	4	154.1	0.15	7	95.37	0.09	10	54.12	0.06
	1.10	2	218.1	0.26	5	141.9	0.14	8	53.01	0.08	11	45.62	0.05
	1.20	3	232.1	0.22	6	67.46	0.11	9	64.46	0.07	12	43.79	0.05
	1.30												
	1.40												
	1.50												

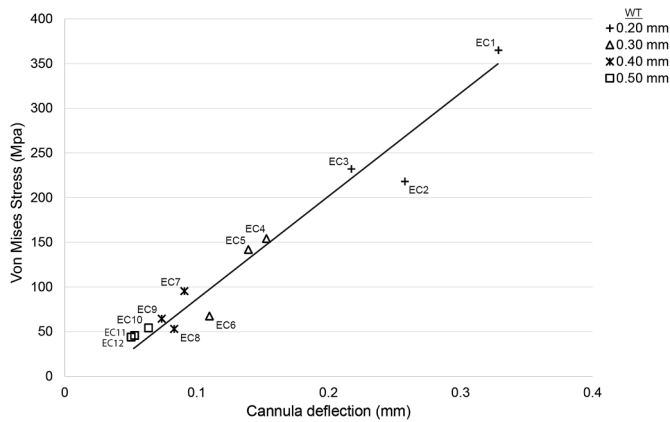


Fig. 7. Overview of the relation between cannula deflection and Von Mises Stress for all twelve experimental conditions from the FEA. The trend line indicates the linear correlation.



Fig. 8. FEA visualization of EC 3, having a clearance of 0.29 mm. The curved course of the stylet inside the cannula and the corresponding Von Mises stress are shown.

is demanded as the tissue penetration depth of radioactive ^{166}Ho used during an interventional procedure is small and entire tumour coverage is required. Next to this, MRI allows for visualization of the administration device, feedback on needle trajectory, tumour location, and

Table 2

Mean absolute errors and standard deviations of positioning accuracy test in XZ-plane and YZ-plane combined for different experimental conditions.

		Orientation angle of stylet (°)			
N = 168		0°	90°	315°	Total
Stylet depth (mm) Number of rotations	1 Mean absolute error $\pm \sigma$	1.16 \pm 0.56	0.43 \pm 0.36	0.58 \pm 0.50	0.72 \pm 0.57
	2 Mean absolute error $\pm \sigma$	0.70 \pm 0.45	0.72 \pm 0.39	0.75 \pm 0.43	0.72 \pm 0.41
	3 Mean absolute error $\pm \sigma$	0.93 \pm 0.54	0.83 \pm 0.48	0.94 \pm 0.67	0.90 \pm 0.56
	4 Mean absolute error $\pm \sigma$	1.44 \pm 0.67	0.92 \pm 0.59	1.14 \pm 0.93	1.17 \pm 0.75
Total		1.06 \pm 0.61	0.73 \pm 0.49	0.85 \pm 0.67	0.88 \pm 0.61

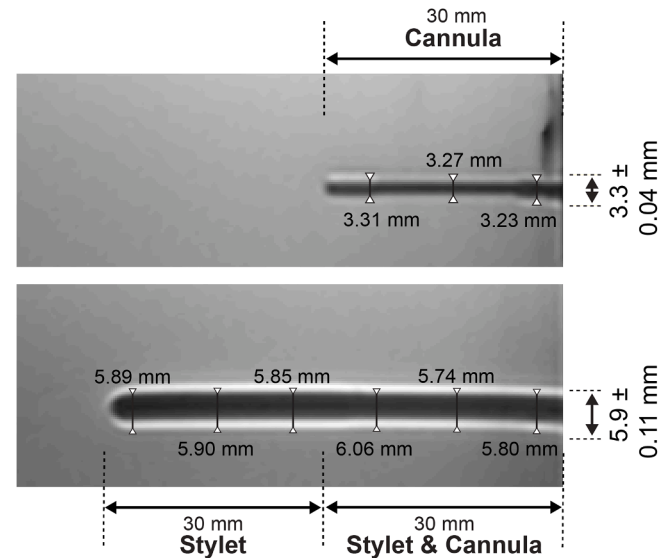


Fig. 9. Artefact visualization and measurements on MRI scan of the cannula (top), stylet (bottom left) and stylet and cannula together (bottom right) in perpendicular orientation towards B0.

Ho-MS quantification. These characteristics contribute to a good foundation for further instrument optimization and demonstrate the potential for precise instrument tracking during brain tumour treatment.

The use of steerable needles in microbrachytherapy creates a potential strengthening of this treatment option. In the brain, this functionality allows for sensitive structure avoidance and multiple target locations can be reached without reinsertion. As opposed to non-holonomic bevel-tip needle steering, proposed in earlier studies [22,25,28], the developed minimally invasive precurved instrument allows for controlled needle trajectories.

The results of the MRI test show that the bioceramic material caused smaller distortions compared to nitinol which is consistent with the magnetic susceptibility values and findings of Matsuura et al. [50]. A more perpendicular orientation of the nitinol stylet towards the

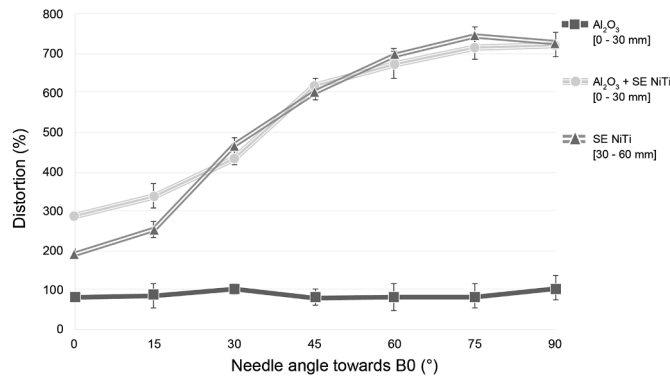


Fig. 10. Material-induced artefact quantification in 3T MRI. Needle angle (°) towards the magnetic field, B0, is shown on the X-axis, the amount of distortion in (%) on the Y-axis.

magnetic field resulted in the largest artefacts due to the maximal susceptibility effect and the radio-frequency (RF) eddy current [51]. Distortions were reduced with a total factor of 3.8 by placing the stylet parallel to B0. When planning the optimal path to the tumour during a clinical procedure, the orientation of the stylet towards the magnetic field should be considered. Further reduction of distortions can be achieved by using a weaker magnetic field [52] or by using a strong diamagnetic coating or filling of the needle [53]. Suitable diamagnetic materials can compensate for the paramagnetic properties of the nitinol stylet. We assume that there will be no differences in artefact size for the same orientation between the straight and curved stylet, as they are both in austenite phase. However, this effect should be investigated in more detail. The distortions of the bioceramic cannula are small because of a slight susceptibility difference with water and therefore the gelatin phantom (97% water) [36]. Besides, no RF-induced eddy currents are present due to the nonconductive behavior [51]. Though, the presence of oxygen ($\chi_{\text{oxygen}} = 0.36 \times 10^{-6}$) [36] in the cannula or the crystal structure and grain size of the alumina oxide may have influenced the distortions [35]. Both the hypointense and hyperintense signals of the bioceramic cannula remained constant regardless of the orientation towards B0. In comparison, the signal void of plastic catheters, with a magnetic susceptibility in the order of -10^{-5} , is small and does not depend on its orientation in the magnetic field [54,55]. Adapting the windowing parameters eventually shows only the hypointense (dark) signal with a diameter corresponding to the outer diameter of the cannula. However, adjusting the relevant parameters could counteract the detection of intracranial structures and lesions. Noteworthy is that the measuring method and the effect of the 3-mm slice thickness may have influenced outcomes and focus was not on quick MRI acquisition. In future experiments, the slice thickness should be reduced and acquisition time should be minimized for eventual clinical procedures.

The ability to locally deliver a substance entails puncturing precision, stylet reach and controllability. Because the Ho-MS suspension leaves the stylet at the distal end, positioning the stylet tip is critical. On some MRI scans disturbances at the tip were found. The occurrence of this blooming-ball shaped void could have been the result of the abrupt variation of the magnetic field intensity at the tip of the needle. This may induce difficulties in precisely localizing the distal tip of the stylet in future experiments. Müller-Bierl et al. reported that a strong diamagnetic coating or filling of the instrument could reduce tip artefacts [53]. Although, earlier research shows that the distal tip is generally located at the centre of the void [56].

Positioning accuracy of the delivery device was assessed by stylet tip location during insertions in homogeneous porcine gelatin, resulting in an accuracy of < 1 mm. It was reported that the absolute error had a tendency to become larger after every rotation, causing a larger stylet depth, which is confirmed by van de Berg et al. [57]. In our research the developed stylet travels over a shorter distance, being less prone to



Fig. 11. Microsphere depots and dose distribution in brain tumour phantom visualized by a multi-gradient echo MRI scan (left) and in Q-suite (19.6% Holmium-165 by mass, fictional specific activity 12 MBq/mg) (right). Both images are merged with the T2W-TSE scan for visualization of the instrument and anatomical tumour reference. The administration device has been inserted into the tumour phantom at different locations following the protocol described in Section 2.2.3. After nine injections the total mean dose is 66 Gy, of which 40% of the tumour volume received a dose of at least 60 Gy.

distortions. In addition, absolute error was influenced by the set orientation of the stylet. A decisive factor concerning variance in both depth and lateral error is a lack of functionality in fixation of the stylet. Variability between manually controlled insertions possibly increases with the absence of fixation. In comparison with currently used biopsy needles, the developed instrument has comparable average placement errors [58]. Noteworthy is that light refraction, surface smoothness of the gelatin blocks and possible differences in phantom stiffness may have influenced measurements.

In the feasibility experiment with Ho-MS a mean dose of 66 Gy was found in the tumour, were 40% of the tumour received a dose of at least 60 Gy. Literature affirms that external beam radiation requires a dose of 60 Gy for an increased survival of patients with malignant glioblastomas without increasing central nervous system toxicity [59]. Since the risk of central nervous system toxicity is actually lower compared to the dose simulations in this study, because of the low tissue penetration depth of the beta radiation of ^{166}Ho , the actually administered radioactivity and the absorbed dose during microbrachytherapy could be increased compared to our simulations. Therefore, studies have to be performed to assess mean dose in relation to therapy effect.

The curvature at the distal end of the stylet allows for a maximum reach of 30 mm, and thus achieving the limit for performing SRS (30 mm in diameter). Dose delivery demonstrated that Ho-MS penetration in the tumour phantom allowed for treatment of tumours with a diameter ≤ 50 mm. Earlier studies showed that tumours up to 52 cm^2 were treated by SRS, making the administration device adequate for larger malignancies as well [31]. However, all tumours have different shapes, sizes, properties and transitions between tumour and brain tissue. This induces untreated parts when Ho-MS injection will be performed with this instrument. A suitable stylet with adjusted tip dimensions, considering tumour size and shape, is critical in every procedure to cover the whole tumour volume. Additionally, optimization of the cannula should be taken into account, considering precise mechanical properties, settings for finite element analysis including a dependent variable for friction, the permitted Factor of Safety and the influence of external loads. For follow-up studies we recommend to incorporate fixation of the stylet at the proximal handle, enlarge clearance between cannula and stylet for both smoother movement of the stylet and reduction of Von Mises stress. RF heating of the stylet during MRI should be assessed and *in-vivo* experiments with animals should be performed for the evaluation of instrument accuracy and dose coverage in a more realistic environment.

5. Conclusion

The instrument for MRI-guided intratumoural administration of radioactive holmium microspheres for treatment of brain malignancies was developed and validated in this work. The prototype is able to precisely reach multiple places in a phantom while having one single access channel and allows for dose delivery of ^{165}Ho -Ms in a suitable tumour in brain phantom. Visualization of the superelastic nitinol stylet and alumina oxide cannula was possible in 3T MRI. The developed prototype showed that precise stylet placement and dose delivery is possible with Ho-MS. It was demonstrated that the developed administration device is potentially able to perform MRI-guided micro-brachytherapy in the brain.

Funding

This work was supported by the Dutch Research Council (NWO) [nr. 15499];

Ethical approval

Not required

Declaration of Competing Interest

J.F.W. Nijssen is inventor on several patents related to holmium microspheres which are assigned to University Medical Center Utrecht Holding BV, Quirem Medical or BASF. He is co-founder and chief scientific officer of Quirem Medical, and has a minority share in the company Quirem Medical. The activities of J.F.W. Nijssen within Quirem Medical are approved and supported by Prof. Dirkjan Masman (Director Technology Transfer Office Radboud university medical center) and Prof. dr. Mathias Prokop (Head of Department of Medical Imaging at Radboud university medical center).

Acknowledgement

The authors would like to thank M. van der Wel (DEMO Central Workshop TU Delft, The Netherlands) for manufacturing the steerable needle and his suggestions during the development phase. The authors wish to acknowledge and thank S. Janbaz (University of Amsterdam, The Netherlands) and K. Narooei (K. N. Toosi University of Technology, Iran) for their thorough input on the finite element model.

References

- [1] Ferlay J, Colombet M, Soerjomataram I, Mathers C, Parkin DM, Piñeros M, et al. Estimating the global cancer incidence and mortality in 2018: GLOBOCAN sources and methods. *Int J Cancer* 2019;144:1941–53. <https://doi.org/10.1002/ijc.31937>.
- [2] Siegel RL, Miller KD, Fuchs HE, Jemal A. Cancer statistics, 2021. *CA Cancer J Clin* 2021;71:7–33. <https://doi.org/10.3322/caac.21654>.
- [3] Liang J, Lv X, Lu C, Ye X, Chen X, Fu J, et al. Prognostic factors of patients with Gliomas-an analysis on 335 patients with Glioblastoma and other forms of Gliomas. *BMC Cancer* 2020;20:1–7. <https://doi.org/10.1186/s12885-019-6511-6>.
- [4] Dirven L, Koekkoek JAF, Reijneveld JC, Taphoorn MJB. Health-related quality of life in brain tumor patients: as an endpoint in clinical trials and its value in clinical care. *Expert Rev Qual Life Cancer Care* 2016;1:37–44. <https://doi.org/10.1080/23809000.2016.1136793>.
- [5] Brown PD, Ballman KV, Cerhan JH, Anderson SK, Carrero XW, Whitton AC, et al. Postoperative stereotactic radiosurgery compared with whole brain radiotherapy for resected metastatic brain disease (NCCTG N107C/CEC-3): a multicentre, randomised, controlled, phase 3 trial. *Lancet Oncol* 2017;18:1049–60. [https://doi.org/10.1016/S1470-2045\(17\)30441-2](https://doi.org/10.1016/S1470-2045(17)30441-2).
- [6] McDermott MW, Sneed PK, Gutin PH. Interstitial brachytherapy for malignant brain tumors. *Semin Surg Oncol* 1998;14:79–87. [https://doi.org/10.1002/\(sici\)1098-2388\(199801/02\)14:1<79::aid-ssu10>3.0.co;2-4](https://doi.org/10.1002/(sici)1098-2388(199801/02)14:1<79::aid-ssu10>3.0.co;2-4).
- [7] Chen AM, Chang S, Pouliot J, Sneed PK, Prados MD, Lamborn KR, et al. Phase I trial of gross total resection, permanent iodine-125 brachytherapy, and hyperfractionated radiotherapy for newly diagnosed glioblastoma multiforme. *Int J Radiat Oncol Biol Phys* 2007;69:825–30. <https://doi.org/10.1016/j.ijrobp.2007.03.061>.
- [8] Huh R, Park YS, Lee JD, Chung YS, Park YG, Chung SS, et al. Therapeutic effects of Holmium-166 chitosan complex in rat brain tumor model. *Yonsei Med J* 2005;46:51–60. <https://doi.org/10.3349/ymj.2005.46.1.51>.
- [9] Klaassen NJM, Arntz MJ, Gil Arranja A, Roosen J, Nijssen JFW. The various therapeutic applications of the medical isotope holmium-166: a narrative review. *EJNMMI Radiopharm Chem* 2019;4:1–26. <https://doi.org/10.1186/s41181-019-0066-3>.
- [10] Ha EJ, Gwak HS, Rhee CH, Youn SM, Choi CW, Cheon GJ. Intracavitary radiation therapy for recurrent cystic brain tumors with holmium-166-chico: a pilot study. *J Korean Neurosurg Soc* 2013;54:175–82. <https://doi.org/10.3340/jkns.2013.54.3.175>.
- [11] Arranja AG, Hennink WE, Denkova AG, Hendrikx RWA, Nijssen JFW. Radioactive holmium phosphate microspheres for cancer treatment. *Int J Pharm* 2018;548:73–81. <https://doi.org/10.1016/j.ijpharm.2018.06.036>.
- [12] Shi Y, Johnsen AM, Di Pasqua AJ. Holmium for use in cancer therapy. *Comments Inorg Chem* 2017;37:281–300. <https://doi.org/10.1080/02603594.2017.1333498>.
- [13] Scott LJ, Yanch JC. Absorbed dose profiles for radionuclides of frequent use in radiation synovectomy. *Arthritis Rheum* 1991;34:1521–30. <https://doi.org/10.1002/art.1780341208>.
- [14] Elschot M, Smits MLJ, Nijssen JFW, Lam MGEH, Zonnenberg BA, Van Den Bosch MAJ, et al. Quantitative monte carlo-based holmium-166 SPECT reconstruction. *Am Assoc Phys Med* 2013;40:1–12. <https://doi.org/10.1118/1.4823788>.
- [15] Bakker R, Bastiaannet R, van Nimwegen S, Barten-van Rijbroek A, Van Es R, Rosenberg A, et al. Feasibility of CT quantification of intratumoral ^{166}Ho -microspheres. *Eur Radiol Exp* 2020;4. <https://doi.org/10.1186/s41747-020-00157-2>.
- [16] Seevinck PR, Seppenwoolde J, De Wit TC, Nijssen JFW, Beekman FJ, van Het Schip AD, et al. Factors affecting the sensitivity and detection limits of MRI, CT, and SPECT for multimodal diagnostic and therapeutic agents factors affecting the sensitivity and detection limits of MRI, CT, and SPECT for multimodal diagnostic and therapeutic agents. *Anticancer Agents Med Chem* 2007. <https://doi.org/10.2174/187152007780618153>.
- [17] De Wit TC, Xiao J, Nijssen JFW, Van Het Schip FD, Staelens SG, Van Rijk PP, et al. Hybrid scatter correction applied to quantitative holmium-166 SPECT. *Phys Med Biol* 2006;51:4773–87. <https://doi.org/10.1088/0031-9155/51/19/004>.
- [18] Bult W, Kroeze SGC, Elschot M, Seevinck PR, Beekman FJ, de Jong HWAM, et al. Intratumoral administration of holmium-166 acetylacetonate microspheres: antitumor efficacy and feasibility of multimodality imaging in renal cancer. *PLoS One* 2013;8. <https://doi.org/10.1371/journal.pone.0052178>.
- [19] Suh JH. Stereotactic radiosurgery for the management of brain metastases. *N Engl J Med* 2010;362:1119–27. <https://doi.org/10.1056/NEJMt0806951>.
- [20] Bactor EM, Stolk P, Kang HJ, Clarke C, Rucker C, Croom J, et al. Precisely shaped acoustic ablation of tumors utilizing steerable needle and 3D ultrasound image guidance. In: Proceedings of the medical imaging 2010: visualization, image-guided procedures, and modeling. 7625; 2010. <https://doi.org/10.1117/12.846092>.
- [21] Burgner J, Swaney PJ, Bruns TL, Clark MS, Rucker DC, Burdette EC, et al. An autoclavable steerable cannula manual deployment device: design and accuracy analysis. *J Med Devices* 2012;6:1–7. <https://doi.org/10.1115/1.4007944>. *Trans ASME*.
- [22] Eng J, Podnar G, Kondziolka D, Riviere CN. Toward effective needle steering in brain tissue. In: Proceedings of the annual international conference of the IEEE engineering in medicine and biology society; 2006. p. 559–62. <https://doi.org/10.1109/IEMBS.2006.260167>.
- [23] Dupont PE, Lock J, Itkowitz B, Butler E. Design and control of concentric-tube robots. *IEEE Trans Robot* 2010;26:209–25. <https://doi.org/10.1109/TRO.2009.2035740>.
- [24] Webster RJ, Okamura AM, Cowan NJ. Toward active cannulas: miniature snake-like surgical robots. In: Proceedings of the IEEE international conference on intelligent robots and systems; 2006. p. 2857–63. <https://doi.org/10.1109/IROS.2006.282073>.
- [25] Webster RJ, Kim JS, Cowan NJ, Chirikjian GS, Okamura AM. Nonholonomic modeling of needle steering. *Int J Robot Res* 2006;25:509–25. <https://doi.org/10.1177/0278364906065388>.
- [26] Webster RJ, Romano JM, Cowan NJ. Mechanics of precurved-tube continuum robots. *IEEE Trans Robot* 2009;25:67–78. <https://doi.org/10.1109/TRO.2008.2006868>.
- [27] Swaney PJ, Burgner J, Pfeiffer TS, Rucker DC, Gilbert HB, Ondrake JE, et al. Tracked 3D ultrasound targeting with an active cannula. In: Proceedings of the medical imaging 2012 image guided procedures robotic interventions and modeling. 8316; 2012. <https://doi.org/10.1117/12.912021>.
- [28] Minhas D, Eng J, Riviere CN. Testing of neurosurgical needle steering via duty-cycled spinning in brain tissue *in vitro*. In: Proceedings of the annual international conference of the IEEE engineering in medicine and biology society. 2009; 2009. p. 258–61. <https://doi.org/10.1109/IEMBS.2009.5334006>. *Eng Futur Biomed EMBC*.
- [29] Rossa C, Sloboda R, Usmani N, Tavakoli M. Estimating needle tip deflection in biological tissue from a single transverse ultrasound image: application to brachytherapy. *Int J Comput Assist Radiol Surg* 2016;11:1347–59. <https://doi.org/10.1007/s11548-015-1329-4>.
- [30] Okazawa S, Ebrahimi R, Chuang J, Salcudean SE, Rohling R. Hand-held steerable needle device. *Trans Mechatron* 2005;10:285–96. <https://doi.org/10.1109/TMECH.2005.848300>.

- [31] Chin LS, Regine WF. Principles and practice of stereotactic radiosurgery. 2nd ed. Springer International Publishing; 2015. <https://doi.org/10.1007/978-1-4614-8363-2>.
- [32] Tanzi M, Farè S, Candiani G. Biomaterials and applications, 506. Elsevier Ltd.; 2019. <https://doi.org/10.1016/b978-0-08-101034-1.00004-9>.
- [33] Maccauro G, Rossi P, Raffaelli L, Francesco P. Alumina and zirconia ceramic for orthopaedic and dental devices. Biomater Appl Nanomed 2011. <https://doi.org/10.5772/23917>.
- [34] Daculsi G. History of development and use of the bioceramics and biocomposites. Springer International Publishing; 2016. https://doi.org/10.1007/978-3-319-12460-5_2.
- [35] Matsuura H, Inoue T, Konno H, Sasaki M, Ogasawara K, Ogawa A. Quantification of susceptibility artifacts produced on high-field magnetic resonance images by various biomaterials used for neurosurgical implants technical note. J Neurosurg 2002;97:1472–5. <https://doi.org/10.3171/jns.2002.97.6.1472>.
- [36] Schneek J. The role of magnetic susceptibility in magnetic resonance imaging: MRI magnetic compatibility of the first and second kinds. Med Phys 1996;23:815–50. <https://doi.org/10.1118/1.597854>.
- [37] Ortech Advanced Ceramics. Alumina Oxide Ceramics Al₂O₃. - 2020. n.d. <https://www.ortechceramics.com/creamic-materials/alumina-ceramics/>; 2020. [Accessed 17 August 2021].
- [38] Trojanowski P, Jarosz B, Szczepanek D. The diagnostic quality of needle brain biopsy specimens obtained with different sampling methods-experimental study. Sci Rep 2019;9:1–7. <https://doi.org/10.1038/s41598-019-44622-4>.
- [39] Mahvash M, Dupont PE. Fast needle insertion to minimize tissue deformation and damage. In: Proceedings of the IEEE international conference on robotics and automation; 2009. p. 3097–102. <https://doi.org/10.1109/ROBOT.2009.5152617>.
- [40] Kapoor D. Nitinol for medical applications: a brief introduction to the properties and processing of nickel titanium shape memory alloys and their use in stents. Johns Matthey Technol Rev 2017;61:66–76. <https://doi.org/10.1595/205651317X694524>.
- [41] Peeters JM, Van Faassen EEH, Bakker CJG. Magnetic resonance imaging of phase transitions in nitinol. J Biomed Mater Res Part A 2007;80:938–45. <https://doi.org/10.1002/jbm.a.30966>.
- [42] van Nimwegen SA, Bakker RC, Kirpensteijn J, van Es RJJ, Koole R, Lam MGEH, et al. Intratumoral injection of radioactive holmium (166Ho) microspheres for treatment of oral squamous cell carcinoma in cats. Vet Comp Oncol 2018;16: 114–24. <https://doi.org/10.1111/vco.12319>.
- [43] Auricchio F, Taylor RL. Shape-memory alloys: modelling and numerical simulations of the finite-strain superelastic behavior. Comput Methods Appl Mech Eng 1997;143:175–94. [https://doi.org/10.1016/S0045-7825\(96\)01147-4](https://doi.org/10.1016/S0045-7825(96)01147-4).
- [44] Abramczyk H, Imiela A. The biochemical, nanomechanical and chemometric signatures of brain cancer. Spectrochim Acta Part A Mol Biomol Spectrosc 2018; 188:8–19. <https://doi.org/10.1016/j.saa.2017.06.037>.
- [45] Forte AE, Galvan S, Manieri F, Rodríguez Y Baena F, Dini D. A composite hydrogel for brain tissue phantoms. Mater Des 2016;112:227–38. <https://doi.org/10.1016/j.matdes.2016.09.063>.
- [46] Thangavel K, Saritaş EÜ. Aqueous paramagnetic solutions for MRI phantoms at 3 T: a detailed study on relaxivities. Turk J Electr Eng Comput Sci 2017;25:2108–21. <https://doi.org/10.3906/elk-1602-123>.
- [47] Seevinck PR, Van De Maat GH, De Wit TC, Vente MAD, Nijssen JFW, Bakker CJG. Magnetic resonance imaging-based radiation-absorbed dose estimation of 166Ho microspheres in liver radioembolization. Int J Radiat Oncol Biol Phys 2012;83: e437–44. <https://doi.org/10.1016/j.ijrobp.2011.12.085>.
- [48] Van De Maat GH, Seevinck PR, Elschot M, Smits MLJ, De Leeuw H, Van Het Schip AD, et al. MRI-based biodistribution assessment of holmium-166 poly(L-lactic acid) microspheres after radioembolization. Eur Radiol 2013;23:827–35. <https://doi.org/10.1007/s00330-012-2648-2>.
- [49] Vente MAD, Nijssen JFW, De Wit TC, Seppenwoolde JH, Krijger GC, Seevinck PR, et al. Clinical effects of transcatheter hepatic arterial embolization with holmium-166 poly(L-lactic acid) microspheres in healthy pigs. Eur J Nucl Med Mol Imaging 2008;35:1259–71. <https://doi.org/10.1007/s00259-008-0747-8>.
- [50] Matsuura H, Inoue T, Ogasawara K, Sasaki M, Konno H, Kuzu Y, et al. Quantitative analysis of magnetic resonance imaging susceptibility artifacts caused by neurosurgical biomaterials: comparison of 0.5, 1.5, and 3.0 Tesla magnetic fields. Neurol Med Chir (Tokyo) 2005;45:395–8. <https://doi.org/10.2176/nmc.45.395>.
- [51] Guermazi A, Miaux Y, Zaim S, Peterfy CG, White D, Genant HK. Metallic artefacts in MR imaging: effects of main field orientation and strength. Clin Radiol 2003;58: 322–8. [https://doi.org/10.1016/S0009-9260\(02\)00540-8](https://doi.org/10.1016/S0009-9260(02)00540-8).
- [52] Budrys T, Veikutis V, Lukosevicius S, Gleizniene R. Artifacts in magnetic resonance imaging : how it can really affect diagnostic image quality and confuse clinical diagnosis ? J Vibroeng 2018;20. <https://doi.org/10.21595/jve.2018.19756>.
- [53] Müller-Bierl B, Graf H, Steidle G, Schick F. Compensation of magnetic field distortions from paramagnetic instruments by added diamagnetic material: Measurements and numerical simulations. Med Phys 2005;32:76–84. <https://doi.org/10.1118/1.1828674>.
- [54] Rubin DL, Ratner AV, Young SW. Magnetic susceptibility effects and their application in the development of new ferromagnetic catheters for magnetic resonance imaging. Invest Radiol 1990;25:1325–32. <https://doi.org/10.1097/00004424-199012000-00010>.
- [55] Wapler MC, Leupold J, Dragonu I, Von Elverfeld D, Zaitsev M, Wallrabe U. Magnetic properties of materials for MR engineering, micro-MR and beyond. J Magn Reson 2014;242:233–42. <https://doi.org/10.1016/j.jmr.2014.02.005>.
- [56] Liu H, Hall WA, Martin AJ, Truitt CL. Biopsy needle tip artifact in MR-guided neurosurgery. J Magn Reson Imaging 2001;13:16–22. [https://doi.org/10.1002/1522-2586\(200101\)13:1<16::AID-JMRI1003>3.0.CO;2-B](https://doi.org/10.1002/1522-2586(200101)13:1<16::AID-JMRI1003>3.0.CO;2-B).
- [57] van de Berg NJ, Dankelman J, van den Dobbelsteen JJ. Design of an actively controlled steerable needle with tendon actuation and FBG-based shape sensing. Med Eng Phys 2015;37:617–22. <https://doi.org/10.1016/j.medengphy.2015.03.016>.
- [58] Mohyeldin A, Lonser RR, Bradley Elder J. Real-time magnetic resonance imaging-guided frameless stereotactic brain biopsy: technical note. J Neurosurg 2016;124: 1039–46. <https://doi.org/10.3171/2015.5.JNS1589>.
- [59] Ziu M, Kim BYS, Jiang W, Ryken T, Olson JJ. The role of radiation therapy in treatment of adults with newly diagnosed glioblastoma multiforme: a systematic review and evidence-based clinical practice guideline update. J Neuro Onc 2020; 150:215–67. <https://doi.org/10.1007/s11060-020-03612-7>.